Bio-Inspired Hierarchical Structures for Contact-Sensible Adhesives

Hong Hu, Duorui Wang, Hongmiao Tian, Qiyao Huang, Chunhui Wang, Xiaoliang Chen, Yuan Gao, Xiangming Li, Xiaoming Chen, Zijian Zheng, Jinyou Shao**

Dr. H. Hu, D. Wang, Dr. H. Tian, Dr. C. Wang, Dr. X. Chen, Dr. X. Li, Prof. X. Chen, Prof. J. Shao*
State Key Laboratory for Manufacturing Systems Engineering, Xi'an Jiaotong University, Xi'an, Shaanxi, China
E-mail: jyshao@xjtu.edu.cn

Dr. H. Hu, Dr. Q. Huang, Dr. Y. Gao, Prof. Z. Zheng*
Laboratory for Advanced Interfacial Materials and Devices, Research Center for Smart Wearable Technology, Institute of Textile and Clothing, The Hong Kong Polytechnic University, Hong Kong SAR, China
E-mail: tczzheng@polyu.edu.hk

Prof. Z. Zheng
Research Institute for Smart Energy, Research Institute of Intelligent Wearable System, The Hong Kong Polytechnic University, Hong Kong SAR, China

Keywords: bio-inspired adhesion, adhesive structure, uneven surface, capacitive sensor, grasping task

ABSTRACT

Bio-inspired structural adhesives that are capable of bonding two objects together have recently found widespread applications in industrial fields, because of their promising reusability and environmental friendliness. However, such adhesives are usually monofunctional and cannot realize real-time detection on the adhesion status, which is important for both biological systems (e.g., Gecko) and engineered mimics. This study reports a new hierarchical structure with the monolithic integration of adhesion and sensing functions, namely, contact-sensible adhesive (CSA). The proposed CSA is composed of mushroom-shaped microstructures on the top layer for providing strong adhesion, and a pillar array sandwiched by a pair of foil electrodes on the bottom layer as a compliant backing and a capacitive sensor. The CSA is not only sensitive to the external pressure, tension, and shear loads, but also shows enhanced adhesion on uneven surfaces, due to the high compliance of

the hierarchical system. As a proof of concept, the as-prepared CSA was applied as a contact interface in a gripper to complete the grasping task.

1. Introduction

Organisms in nature have evolved many unique functions and survival skills, which serve as inspiration for the development of functional materials, structural design, and mechanical engineering.[1, 2] In recent decades, researchers have paid considerable attention to the adhesive pads of geckos, because they enable a reliable, controllable, and repeatable attachment (or detachment) function on almost any surface regardless of the morphology (rough or smooth), wettability (hydrophilic or hydrophobic) and posture (slant, vertical or inverted).[3, 4] Geckos' adhesion, as demonstrated by Autumn et al.,[5] originates from the highly branched hierarchical structures on the toe pads that accumulate van der Waals interactions at atomic scale up to roughly 100 kPa at the scale of pad area (the capillary force[6, 7] and the acid-base interaction[8] may be also strong in a certain environment). By mimicking these biological structures, a variety of bio-inspired intermolecular-force-based adhesive materials have been developed (which are also called dry adhesive, since they are not tacky and are pressure sensitive [9, 10]). Such materials have been demonstrated to be very effective in a wide range of applications from biomedical devices,[11-13] microfluidics,[14] transfer printing,[15, 16] smart grippers,[17-23] to wall-climbing robots.[24, 25]

To date, strong adhesion can be achieved in manufactured adhesives by employing delicate structures of different shapes (e.g., pillar,[26] wedge,[27] spatula,[28] micro-suction,[29] funnel,[30] and mushroom[31-35]) and materials (e.g., polyurethane,[29] polyvinylsiloxane,[31] silicone rubber,[33, 36] hydrogels,[37] and nano composites[12]) with homogeneous, layered[38-40] and even gradient material properties.[41-43] Nevertheless, this is a passive strategy due to the lack of detection or feedback on the contact interface. In contrast, biological systems use the so-called

active strategy to realize a fast adhesion-based locomotion by sensing the contact status in real-time.[9] The gecko's attachment system is an example, in which the tactile sensing, neuromodulation, and muscle's actuation enable an active adhesion that can be alternatively turned "on/off".[18, 19, 37, 44] Recently, Kalantari et al.[45] introduced contact sensors behind a manufactured dry adhesive to indicate the quality of the adhesive's engagement with the substrate in climbing robot and air vehicle. This method of assembling auxiliary machine parts in the attachment system implies the practical importance of the sensing function, and is technically a remedy for the existing structural design of monofunctional adhesion.[45, 46] However, it may also increase the complexity of the system and may sacrifice the compliance of the bio-inspired adhesives (if the adhesive and sensor are taken as one), which is usually required in soft robotics.

Benefiting from the development of flexible electronics, rapid and highly sensitive tactile function has been achieved in thin film devices by various approaches on the basis of the field-effect transistors, sensing materials,[47] or structures.[48] However, as surface adhesion is not a crucial property concerned by researchers in this field, there are relatively few investigations on active adhesion together with the dynamical detection of interface contact (or force). Kim et al.[12] prepared conductive dry adhesives with 1D-2D hybrid carbon nanocomposites, enabling a stretchable, metal-free, and all-in-one component for measuring electrocardiogram (ECG). However, this type of material and structural design only produces an electrode without any sensing functions. Drotlef et al.[49] proposed another approach by attaching a flexible strain sensor on the backside of a skin-adhesive film to precisely monitor human physiological signals. Although this device is sticky with excellent biocompatibility and can also response to pressure, it might be faced with a challenge to have a complete estimation of the contact when some other forms of loads, e.g., lateral load, are involved.

Inspired by the external morphology and internal nerves of Gecko's attachment system, this work presents a hierarchical structure for the realization of a contact-sensible adhesive (denoted as CSA), which is a monolithic integration of dry adhesion and contact sensing. The CSA is composed of two-layer structures with mushroom-shaped structures on the top for providing a strong adhesion, and a compliant and contact-sensible backing on the bottom. As such, the CSA is advantageous for sensing different types of external loads such as pressure, tension, and shear loads, and also exhibits high surface adaptability, attributed to the high compliance of the hierarchical system.[50, 51] It is envisioned that such a novel CSA could have promising applications, especially for surface force detection or adhesion on an uneven surface.

2. Results and discussion

2.1 Structural design of CSA

The structural design of CSA was inspired by the gecko's attachment system that consists of hierarchically fine structures and many nerve cells (**Figure 1a**). To monolithically integrate these two functions in CSA, mushroom-shaped adhesive structures were engineered on a capacitive force sensor (Figure 1b). The mushroom-shaped structure with a thin plate on top of a pillar is a unique contact element that can outperform many other shapes in dry adhesives because of its flattened interfacial stress,[31, 52] small-scale crack bridging behavior,[53] friction contribution,[54] suction effect,[55] and self-cleaning performance to prevent any possible dust.[56] As a backing of the adhesive structures, pillars were sandwiched by a pair of foil electrodes, forming a capacitive force sensor on the bottom.[13, 57] When external loads (L) were applied on the CSA, the deformation of pillars on the bottom layer led to the change in electrode distance and, thus, the change in capacitance value (C). For example, the capacitance increased under a pressure (L_n>0, ΔC>0) or a shear load (L_s>0, ΔC>0), while it decreased under a tension load (L_n<0, ΔC<0) (ΔC denotes the change in capacitance value,

and the subscripts ‘n’ and ‘s’ represent the normal and shear load, respectively (Figure 1c). Scanning electron microscope (SEM) image of a representative sample shows the two-layer structures (Figure 1d). The structures were made of polydimethylsiloxane (PDMS), while the electrodes were two ~20 μm thick PET foils coated with 50 nm thick Au films (Experimental Section, and Supporting Information, Figure S1). The structural dimensions can modulate the adhesion and sensing performance. A relatively low aspect ratio α of about 1.26 (the ratio of height h to diameter D, *i.e.* $\alpha=h/D$) was adopted for the mushroom-shaped structures, as a small α decreases the risk of structural collapse[58, 59] and buckling,[60] either of which could weaken the interfacial adhesion. Simultaneously, the structures on the top layer were packed in a higher duty ratio β (the ratio of diameter D to center-to-center distance l, i.e., $\beta=D/l$) than the bottom layer. Such a structural design provided more adhesive structures for the requirement of strong adhesion. More importantly, it increased the compliance of the backing[51] (high α and low β) and the sensitivity of the sensor (the relationship between the sensitivity and geometrical dimensions of the structures on the bottom layer will be discussed in detail later). For this sample, the dry adhesion effect generated on a nominal area of about 1.5 cm^2 (Figure 1e I) can suspend a 500 g weight in both the normal and lateral directions (Figure 1e II and 1e III, respectively). The initial capacitance value (C_0) detected via a multimeter indicated the normal function of the capacitor (Figure 1e IV).

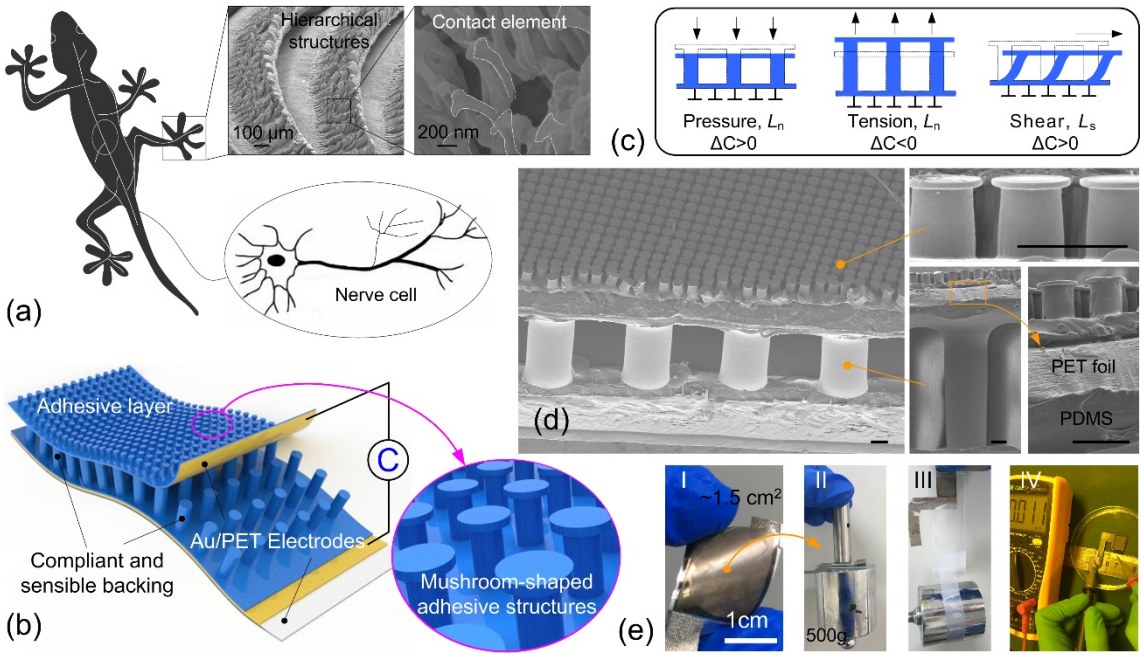

Figure 1. Schematic illustration of bio-inspired hierarchical structures for enabling CSA. a) Gecko's kinesthetic system consisting of its sticky pads for adhering to target surfaces and underlying nerves for perceiving and feeding-back contact status. b) Structural design of CSA with mushroom-shaped adhesive structures on the top layer and pillars on the bottom layer. A capacitive force sensor is formed by introducing two foil electrodes to sandwich the pillars on the bottom layer. c) Different deformation behaviors of structures by pressure, tension, and shear load, respectively. Electrode distance is considered as the single factor determining the change in capacitance value. d) SEM images of CSA. The scale bar is 25 μm. e) Photograph of a CSA sample (I), its adhesion performance in normal (II) and lateral directions (III), and detectable capacitance value by a multimeter (IV). The weight is 500 g.

2.2 Demonstration of integrated adhesion and sensing

To demonstrate the integrated functions of adhesion and sensing of the CSA, the force and capacitance values were measured simultaneously in the loading/unloading process. **Figure 2a** illustrates the schematic of the measurement setup, where a CSA sample (area: ~1.5 cm^2) was glued on the free end of a double cantilever beam (DCB) with its adhesive layer facing a smooth glass slide, which was also fixed on a DCB. The load was obtained by checking the deflection of DCB, while the capacitance was recorded by a semiconductor analyzer (Experimental Section). Figure 2b shows the normal load L_n and relative change in capacitance, $\Delta C/C_0$, as a function of time. $\Delta C/C_0$ increased during loading and decreased during the unloading process (portion between A and B points). The positive maximum value of L_n indicated the preload, L_{pre}≈14.9 kPa. Subsequently (after B point), the normal load

changed from pressure to tension (L_n<0), and decreased gradually to a negative maximum value of -28.7 kPa (normal pull-off strength, σ_p), at which point the adhesion failed (C point). Moreover, $\Delta C/C_0$ also decreased below zero and reached its negative maximum value of -0.31, implying a rapidly detectable capacitive response. Figure 2c shows the time-resolved $\Delta C/C_0$ curves in response to shear load (L_s) with different shear velocities (v_s=1, 2, 3 mm/s). The peak of each L_s-t curve represented the adhesion failure, and the corresponding values of L_s indicated the shear pull-off strength (τ_p), which was roughly 43.3 kPa for v_s=3 mm/s, while it decreased to 32 kPa for v_s=1 mm/s. For different shear velocities, the capacitance curves all followed the change trend of the shear load. These results demonstrate the successful integration of adhesion and sensing functions in the CSA. Specifically, the CSA responded to both normal and shear loads, which could not be achieved by the structural designs reported previously.[13, 49] To further examine the stability of the integrated functions, the time-resolved capacitive response was compared with the applied load in cyclic loading and unloading processes (Figure 2d). For three different loading conditions, where (I) adhesion was and (II) was not always maintained under a normal (tensile) load, and (III) adhesion was maintained under a shear load, both the capacitive response and the load showed high stability without any significant decay. Further statistical analyses also showed that the relative standard deviation (RSD) in the repeated loading cycles was smaller than 0.5% (Figure S2 and S3, Supporting Information). Such high stability implied the reversible adhesion and restorable sensing functions of the CSA.

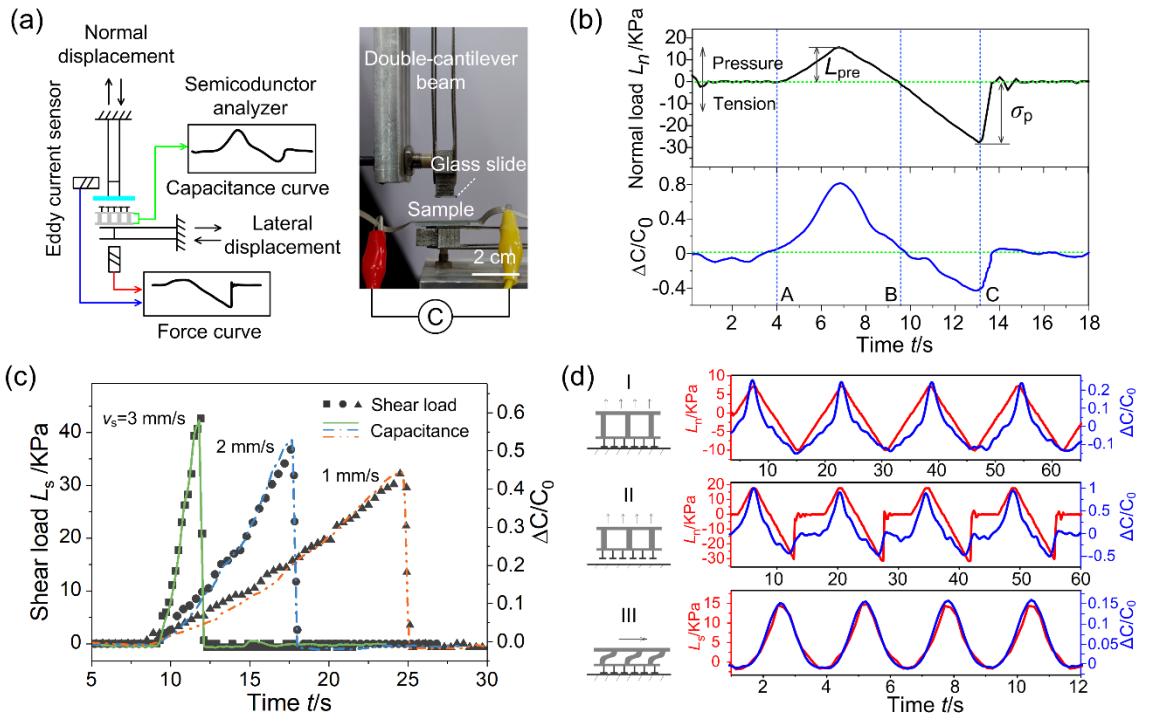

Figure 2. Characterization of integrated functions of adhesion and sensing of CSA. a) Schematic and photograph of the home-built measurement set-up. The normal and lateral loads can be obtained from the vertically and horizontally mounted double-cantilever beams, respectively. b) L_n-t and $\Delta C/C_0$-t curves obtained in normal loading and unloading processes. The curves are divided into two parts by the green dotted line, above which structures are in a compressive state by the pressure, while below it, they are in a stretched state by the tension load. The points A, B, and C represent the beginning of the loading, unloading, and adhesion failure, respectively. c) L_n-t and $\Delta C/C_0$-t curves obtained for different velocities of shear loads. The peaks of these curves correspond to adhesion failure, after which both the sensor output and load reduce to zero quickly. d) Time-resolved capacitive responses under repeated loading cycles in different cases, where (I) adhesion is, and (II) adhesion is not maintained under a normal load, and (iii) adhesion is maintained under a shear load, respectively.

2.3 Quantitative law between sensitivity and structural dimensions

It is practically significant to establish a quantitative law between the key technical parameter, the sensitivity (S), of the capacitive force sensor (one of the functions of the backing) and the structural dimensions. Here, three CSA samples with different structural dimensions (height, h, diameter, D, and center to center distance, l) were prepared and their SEM images (labeled as I, II, III) are displayed in **Figure 3a**. Figure 3b-3d shows the relative capacitance variation ($\Delta C/C_0$) in response to the tension, pressure, and shear load, respectively. The slope for the discrete data is defined as the sensitivity, given by $S = \delta(\Delta C/C_0)/\delta L$. [57] For the simplest case of structures in the stretched state by the tension

load, the $\Delta C/C_0$ changed linearly with the tension load ($-L_n$) for all samples (Figure 3b). However, in the case of pressure load, the $\Delta C/C_0$-L_n curves showed different responses to the pressure load in different ranges (Figure 3c). For example, the sensitivity of sample III significantly increased from 0.007 kPa^{-1} to 0.139 kPa^{-1} with an enhancement of approximately 20-fold at L_n=8.7 kPa. Note that the pressure load for the initiation of this enhancement was very close to the so-called Euler load of the bottom-layer structures, L_E≈7.6 kPa (green dotted line, in Figure 3c)[61, 62]. Hence, it can be deduced that the complicated response of the CSA sample to pressure load was a result of the structural buckling behavior. Once buckling occurs in the loading process, the compliance of the structures increases due to the additional elastic bending energy,[63] thus causing a stronger response for the capacitive sensor. In the case of shear load, $\Delta C/C_0$ also showed a simple linear relation to a wide range of shear loads (Figure 3d).

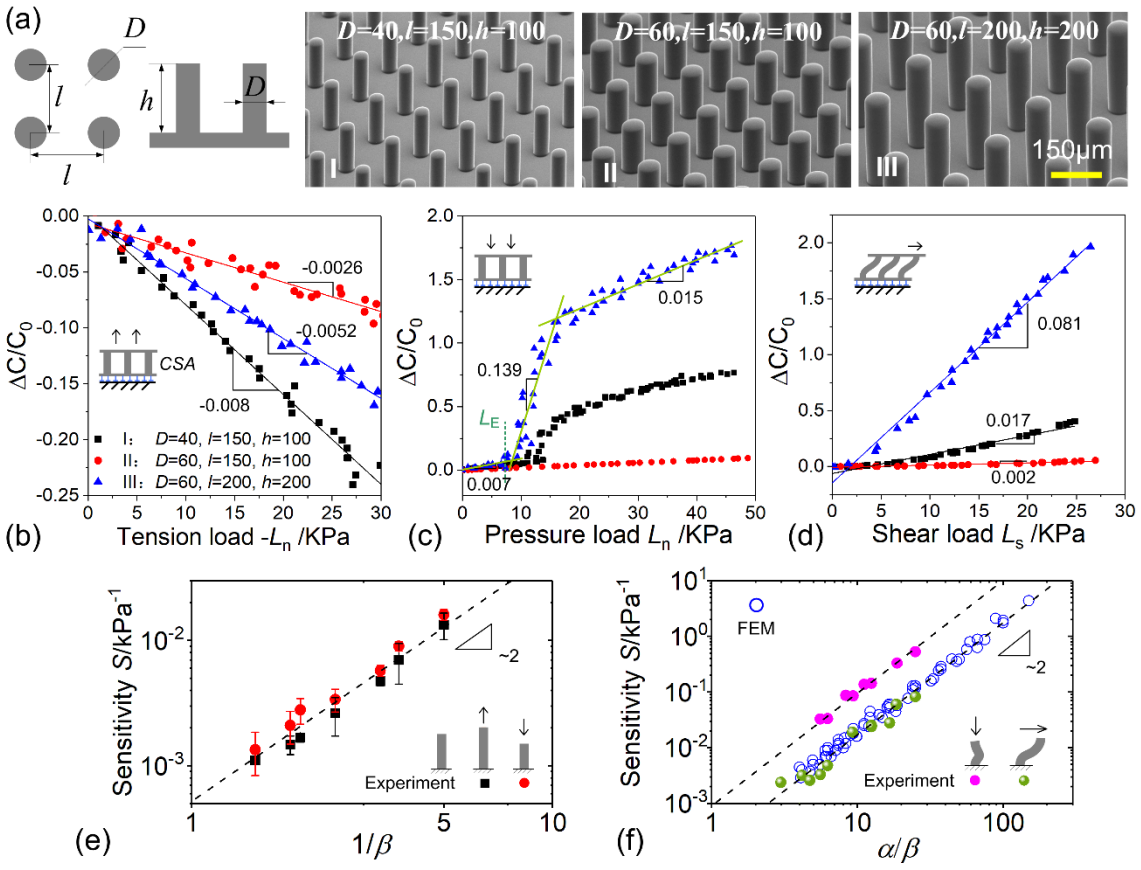

Figure 3. Characterization of capacitive response of CSA to different external loads and its dependence on structural dimensions. a) SEM images of three CSA samples having different

diameters D, heights h, and center-to-center distances, l. b)-d) Relative change in capacitance ($\Delta C/C_0$) as functions of tension ($-L_n$), pressure (L_n), and shear loads (L_s), respectively. Under a tension load, $\Delta C/C_0$ changes linearly with L_n, while under a pressure load, the capacitive response is complicated due to the buckling behavior. For the shear load case, $\Delta C/C_0$ also changes linearly over a wide range of shear load. e) and f) Quantitative law between sensitivity (S) and structural dimensions. S can be expressed as a scaling power law of two dimensionless geometrical parameters, $1/\beta$ and α/β, corresponding to the upstanding and curved (buckling or deflection) posture of the structure, respectively, with a power value of 2. The solid and open symbols refer to the experimental and FEM results, respectively, while the dotted lines represent the formular prediction.

The results shown in Figure 3a-3d also indicated a strong dependence of the sensing performance on the structural dimensions. Next, it was further demonstrated that this dependence can be explicitly described by two simple power law scaling relations. To achieve this, the capacitive responses of more CSA samples were characterized (Supporting Information, Figure S4-S7). Through the dimension analysis[64] (Supporting Information, Supplementary Notes S2), the sensitivity, S, can be fully determined by the material property (elastic modulus, E), and the two dimensionless geometrical parameters, *i.e.*, aspect ratio, α, and duty ratio, β. S was found to follow a scaling power law of $1/\beta$, as $S \sim (1/\beta)^2/E$, for structures in upstanding posture, while it followed a scaling power law of α/β, as $S \sim (\alpha/\beta)^2/E$, for the structures in buckling or deflection postures. Note that, the first scaling relation can be directly derived under the linear approximation of a capacitive sensor (Equation S4, Supporting Information), while the second scaling relation required fitting on a series of numerical results (Figure S8 and S9, Supplementary Notes S3, Supporting Information).

Figure 3e and 3f present the comparison between the experimentally obtained S values and the prediction by the two scaling relations, respectively. The high consistency between them demonstrated the correctness of the formulas, which could facilitate the design of future devices for the purpose of obtaining specific sensitivity of the CSA. Generally, the sensitivity in response to the normal load is higher than that to the shear one, because the compression or

stretch deformation can induce the change in electrode distance easier than the deflection. The increasing tendency of S with respect to α/β or $1/\beta$ suggested that structures with high aspect ratios and low duty ratios could yield highly sensitive capacitive sensors either in normal or shear load cases. However, excessively high value of α/β is not always preferred for engineering high-performance CSA samples. This is because sufficient mechanical strength and damage tolerance of the structures on the bottom layer are also essentially required, since they serve as the backing of the adhesive layer.[60]

2.4 Enhanced adhesion of CSA on uneven surface.

The above results demonstrated the integrated functions of adhesion and sensing on a flat surface. However, in most applications, the target surface is uneven and the structural adhesion can be largely reduced.[65, 66] Many previous studies have demonstrated that an effective way to enhance the adhesion on uneven surfaces is to employ highly compliant materials[67] and structures.[68] To examine whether the introduced rigid component (i.e., the metal-coated PET foil with elastic modulus nearly 3-order of magnitude larger than the silicone) affected the compliance as well as the adhesion performance of CSA against the uneven surface, the normal pull-off force of a CSA sample (area: ~4 cm^2) was compared with that of a single-level control sample on an acrylic substrate with periodically-distributed spherical asperities (cross section of the uneven substrate is shown in Figure S10). To exclude the possible influence of the backing layer thickness on the adhesion performance,[69] the total thicknesses of these two samples in the experiment were comparable (Figure S11, Supporting Information). As shown in **Figure 4a**, the pull-off force, F_p, increased in the early stage with increase in the preload, F_{pre}, and eventually reached saturation.[19, 70] This is because a large preload extends the actual contact area on an uneven surface, causing more adhesive structures to function. However, partial structures underneath the asperities are likely to be compressed heavily (or buckle) with significant adhesion loss by the large preload.[60]

Therefore, the saturated pull-off force is a result of the competition between these two effects. In the present experiments, the adhesion of CSA sample (F_{pull}≈7.8 N) was ~3.7 times larger than that of the single-level control sample (F_{pull}≈2.1 N) as the preload increased up to 8~10 N.

Experimental results indicated stronger adhesion of CSA sample than that of single-level control sample. To further demonstrate that this adhesion enhancement was due to the high compliance of the structured backing, a simple FEM simulation was performed here for investigation of the interfacial contact stress (Figure 4b I, details are included in Experimental Section). In the simulation, a spherical asperity was indented to a structured and bulk backing by a load of ~25 kPa, which corresponded to the case of the CSA sample and the control sample (Figure 4b II and 4b III). The contact interface and contact stress (σ_c) were then obtained (Figure 4c). The CSA sample displayed a deeper indentation and larger contact length than the control sample (Figure 4c I), because of the greatly reduced effective modulus of the structures on the bottom layer. For the single-level control sample, σ_c followed the Hertz contact theory (black line, Figure 4c II).[71] In contrast, σ_c fluctuated for the CSA, and reached a peak at the pillar position and a valley at the bridge (red line, Figure 4c II).[51, 60] Since only the structures with contact stress less than the buckling limit can contribute to the adhesion,[10] the effective adhesive area, A_{eff}, is defined as the contact region where the contact stress is smaller than the Euler limit, i.e., $\sigma_c<L_E$, where L_E≈0.27 MPa is the calculated Euler load for the array of mushroom-shaped structures (dotted blue line, Figure 4c II). Then, the comparison of the pull-off forces between the two samples may be given by a scaling relation as follows:

$$\frac{F_{pull}^{CSA}}{F_{pull}^{s}}=\frac{A_{eff}^{CSA}}{A_{eff}^{s}}\approx\frac{r_C^2}{r_B^2-r_A^2}=3.34$$

where the superscript refers to the CSA and the single-level control samples, respectively, r_A=614 μm, r_B=1054 μm and r_C=1567 μm indicate the r values at which $\sigma_C^S = L_E$, $\sigma_C^S = 0$,

and $\sigma_C^{CSA} = 0$ (only a small fraction of the σ_c curve for the CSA was beyond L_E and, thus, was neglected). The simulation predicted a 3.34-fold enhancement in adhesion for the CSA sample in comparison with the control sample, which was in good agreement with the experimental results (~3.7-fold). Since the increased A_{eff} is a result of the structured backing with reduced E_{eff},[50] it can be deduced that the CSA still maintained high compliance even though some rigid components (PET electrodes) were introduced to form a capacitive force sensor. Notably, it was further found that the CSA sample outperformed the control sample in adhesion on a planar glass slide (Figure S12, Supporting Information). This result also indicated the high compliance of the CSA, which can reduce the influence of possible misalignment in the flat-to-flat measurement configuration on the adhesion performance.

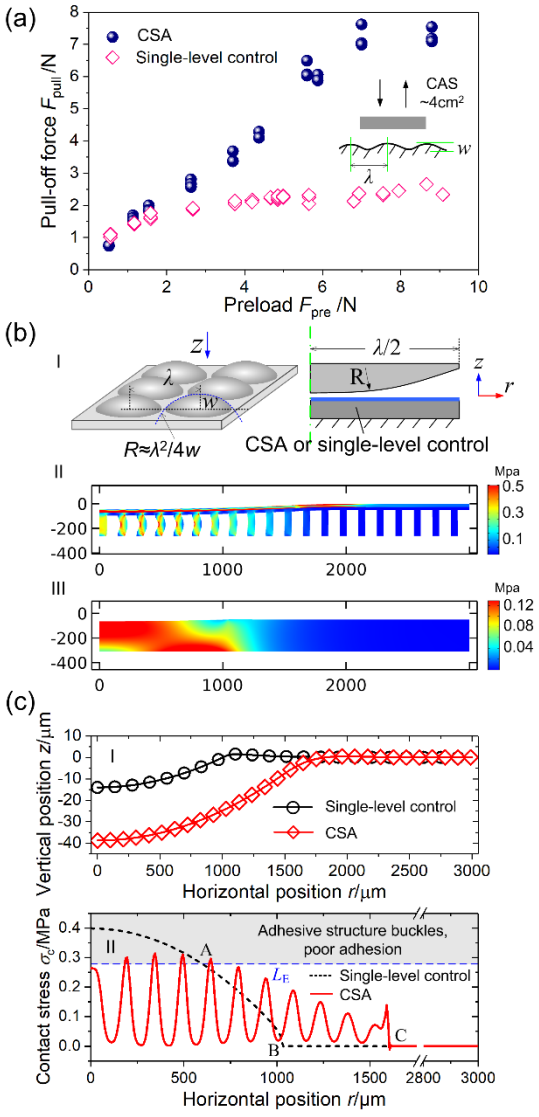

Figure 4. Adhesion of CSA on uneven surface. a) Pull-off force as a function of preload for CSA and single-level control samples, respectively. b) Simulation of a spherical asperity indented onto structured and solid backings under a preload of ~25 kPa, which corresponds to the CSA and control samples, respectively. The length unit is μm. c) Contact length and contact stress distribution at interface. Due to the high compliance, the CSA sample has a larger indentation depth and contact length compared to the control sample. As the structures with compressive stress beyond the buckling limit, L_E, can only provide poor adhesion, the effective adhesive area for CSA ($r<r_C$) is larger than that for the single-level control sample ($r_A<r<r_B$). The dotted blue line stands for the L_E value of the mushroom-shaped structures.

2.5 Application of CSA in grasping task

Finally, to demonstrate the potential application of the CSA, grasping experiments were performed on difficult-to-grasp objects. **Figure 5a** presents the schematic of a typical gripper device, on which a ~1.5 cm^2 sized CSA sample was glued as a contact interface. Successful grasping can be achieved when the lateral force (f) induced by the normal pressure (N) balances the weight of the object (G). To increase the difficulty, a fragile egg was selected as the object and a weight of 300 g was glued on it. The limit normal force (N_{broken}) for the shell fragmentation or breakage is about 6~7 N, suggesting a dangerous value of $\Delta C/C_0$ for the grasping task, $V_d \approx 0.1$, according to the sensitivity (Supporting Information, Figure S13). The photographs and the corresponding sensor outputs in real time ($\Delta C/C_0$-t curve) of the grasping process for three different normal loads are shown in Figure 5b and 5c, respectively. In Figure 5b, the positions of the gripper and the egg are depicted by the blue and yellow lines. The symbols of rectangle, sphere and diamond in Figure 5b and 5c represent the moment when the photographs were captured. For a large normal load ($\Delta C/C_0 = 0.064 < V_d$), the egg could be picked up steadily. Both the blue and yellow lines moved upwards (Figure 5b I; Movie S1, Supporting Information). Note that, the sensor output during the lifting process was higher than that with only the application of normal load, because of the generation of lateral force (the rectangle and sphere symbols, Figure 5c I). For a small normal load ($\Delta C/C_0 = 0.025$), the lateral force could not support the object, resulting in slippage during the grasping process. The blue line moved upwards, but the yellow line did not (Figure 5b II, Movie S2, Supporting

Information). The $\Delta C/C_0$-t curve presented a slow fall until the total separation (the arrow, Figure 5c II). This phenomenon suggests that the gripper with the CSA can detect the possible slip based on the slow fall of the $\Delta C/C_0$-t curve and then increase the normal load appropriately to prevent it. As shown in Figure 5b III, the gripper could not lift the egg at first because a small normal load was again applied ($\Delta C/C_0$=0.01), resulting in the slip. The yellow line did not follow the blue line moving upwards. Then, by increasing the normal load with the $\Delta C/C_0$ up to about 0.08 (Figure 5c III), the slip trend stopped, and both the blue and yellow lines moved upwards, indicating a successful grasping process (Movie S3, Supporting Information).

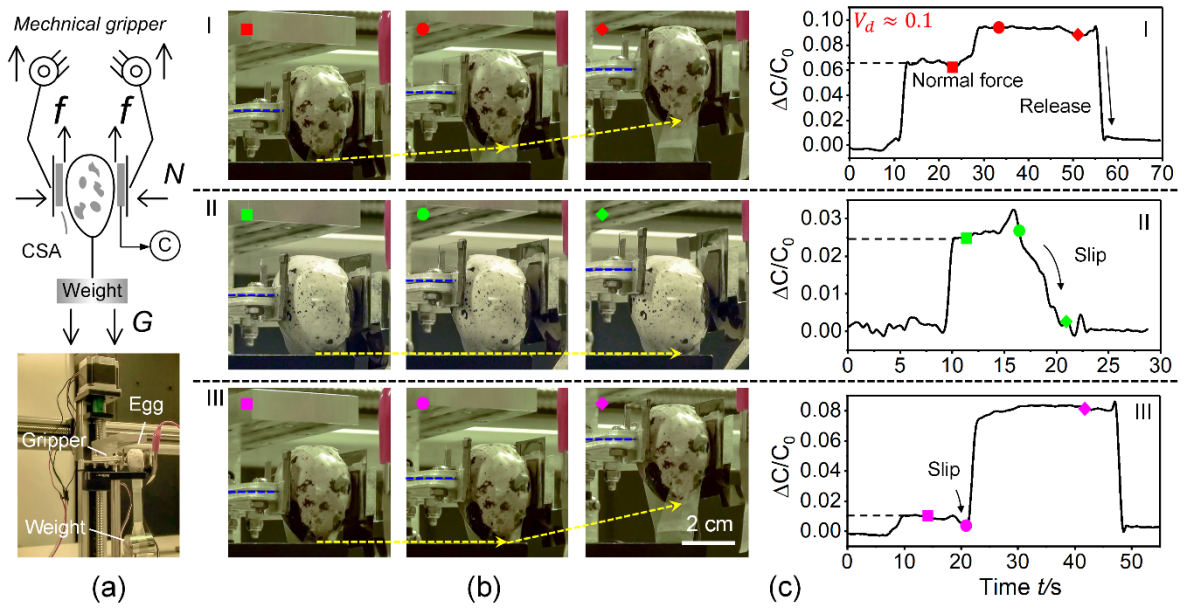

Figure 5. Proof-of-concept of CSA as a contact interface introduced in a mechanical gripper for a grasping task. a) Schematic and photograph of a gripper using CSA to contact with the object (fragile egg with a 300 g weight glued on it). b) Photographs showing grasping process for three cases of different normal loads. The blue and yellow lines denote the position of the gripper and the egg, respectively. In a steady grasping process, both lines move upwards. If the slip occurs, the yellow line does not follow the upward movement of the blue line. c) capacitive response of $\Delta C/C_0$ as function of time corresponding to the three cases in b). The fast drop of $\Delta C/C_0$ indicates the release of the object, while its slow fall indicates the slip. The symbols of rectangle, sphere, and diamond correspond to the moment when the photograph in b) is captured.

3. Conclusion

In this work, a bio-inspired hierarchical structure was developed for the realization of contact-sensible adhesives (CSA). This structure was composed of mushroom-shaped units as a strong adhesive layer on the top, and a pillar array sandwiched by a pair of foil electrodes on the bottom to function as a compliant backing and a capacitive sensor in response to external tensile, compressive, and shear loads. The experimental results demonstrated the integration of adhesion and contact sensing functions, and a quantitative law (scaling power law in power of 2) was established between the sensitivity and the structural dimensions. Furthermore, the CSA showed stronger adhesion (roughly 3.7-fold enhancement) on an uneven surface compared with the single-level control sample, due to the high compliance of the hierarchical structures. The potential application of the CSA was also evaluated by using it as the contact interface in a gripper, which ensured the safety of the object and prevented a possible interface slip. It should be pointed out that the proposed structural design is not limited to embedding a single sensor in the backing. By using a patterned electrode to form a capacitive force sensor array, the CSA may be capable of not only adhering to the target surface, but also detecting the position-dependent contact status, which is usually generated in grasping tasks on objects with uneven or curved profile.

4. Experimental Section

Fabrication of CSA: The mushroom-shaped structures on the top and the pillars on the bottom of CSA sample were both fabricated by the conventional modeling process. The template (Si) with micro holes for pillars was fabricated by photolithography and etching, while that for the mushroom-shaped structures can be obtained either by the double-side exposure method reported by Wang et al., [33] or by producing an undercut in a sacrificial layer as reported by Sameoto et al.[72, 73] The electrodes for the capacitive force sensor on the bottom were fabricated by sputtering Au (50 nm thick) on a PET foil (20 μm thick). The CSA can be

achieved by assembling the top- and bottom-layer structures. Details of the fabrication are included in the Supporting Information (Figure S1).

Characterization of adhesion and sensing properties of CSA: The capacitive responses of the CSA to normal and shear loads were characterized using a home-built apparatus (Figure 2a).[19] The CSA sample was glued on the free end of a double cantilever beam (DCB) with its adhesive layer facing a smooth glass slide, which was also fixed on another DCB. The spring constant of the two DCBs was 900 N/m. The vertical and lateral movements of the DCB can apply the normal and shear loads on the sample, respectively. The movement was controlled by a motorized translation stage (PI Gmbh & Co. M-531.DD, 100 nm resolution). The deflection of the DCB was measured by an eddy current displacement sensor (Waycon) with a high resolution of 30 nm. Its output signal was further recorded by a data acquisition system (LABVIEW, 200 Hz sampling frequency).[33] Finally, the force value was obtained by careful calibration, and the stress value was calculated by dividing the force by the nominal sample area. The capacitance value was recorded by a semiconductor analyzer at 100 kHz (B1500A, Agilent).[57]

Finite Element Method (FEM) simulation: FEM model was established with the commercial software, ABAQUS, to study the contact stress at the interface between an uneven surface and a CSA sample or a single-level control sample. When an uneven surface with periodically distributed spherical asperities with center-to-center distance λ=3.2 mm and peak-to-valley distance w=0.9 mm (cross section of this uneven surface is shown in Figure S10, Supporting Information) was indented onto the sample, the interfacial stress should also be periodic. Thus, only the space near a single asperity was modeled. The simulation only considered the deformation of the backing layer. It was further assumed that the 3-dimensional problem can be simplified without any significant accuracy loss by an axisymmetric geometry. The asperity was set as a spherical rigid part with a radius of roughly $R \approx \lambda/4w$. As a metal-coated PET foil was inserted between the adhesive structures on the top layer and the backing of the

CSA sample, the material type for this sample was set as, from top to bottom, PDMS film, PET film, and PDMS pillars, respectively. The thicknesses of the PDMS film and PET film were 5 μm and 20 μm, while the height, width, and center-to-center distance of the PDMS pillars were 270 μm, 50 μm, and 150 μm, respectively. For the single-level control sample, the geometry was a bulk solid of 300 μm height. All the materials in the simulation were assumed to be isotropic and linearly elastic. The elastic modulus values of PDMS and PET were set as 3.5 MPa and 4 GPa, respectively. The bottom boundary was fixed, while a downwards load of 25 kPa was applied on the asperity.

Supporting Information
Supporting Information is available from the Wiley Online Library or from the author.

Acknowledgements
H. H. and D. W. contributed equally to this work. The authors acknowledge the funding support from NSFC under grants No. 52025055 and 91323303.

Conflict of Interest
The authors declare no conflict of interest.

References

[1] E. Arzt, H. Quan, R.M. McMeeking, R. Hensel, *Prog. Mater. Sci* **2021**, *120*, 100823.

[2] Y. Chen, J. Meng, Z. Gu, X. Wan, L. Jiang, S. Wang, *Adv. Funct. Mater.* **2020**, *30*, 1905287.

[3] Y. Tian, N. Pesika, H. Zeng, K. Rosenberg, B. Zhao, P. McGuiggan, K. Autumn, J. Israelachvili, *Proc. Natl. Acad. Sci. U. S. A.* **2006**, *103*, 19320.

[4] P.H. Niewiarowski, A.Y. Stark, A. Dhinojwala, *J. Exp. Biol.* **2016**, *219*, 912.

[5] K. Autumn, Y.A. Liang, S.T. Hsieh, W. Zesch, W.P. Chan, T.W. Kenny, R. Fearing, R.J. Full, *Nature* **2000**, *405*, 681.

[6] C.T. Mitchell, C.B. Dayan, D.-M. Drotlef, M. Sitti, A.Y. Stark, *Sci. Rep.* **2020**, *10*, 19748.

[7] G. Huber, H. Mantz, R. Spolenak, K. Mecke, K. Jacobs, S.N. Gorb, E. Arzt, *Proc. Natl.*

Acad. Sci. U. S. A. **2005**, *102*, 16293.

[8] S. Singla, D. Jain, C.M. Zoltowski, S. Voleti, A.Y. Stark, P.H. Niewiarowski, A. Dhinojwala, *Sci. Adv.* **2021**, *7*, eabd9410.

[9] L. Heepe, S.N. Gorb, *Annu. Rev. Mater. Res.* **2014**, *44*, 173.

[10] P.Y. Isla, E. Kroner, *Adv. Funct. Mater.* **2015**, *25*, 2444.

[11] M.K. Kwak, H.-E. Jeong, K.Y. Suh, *Adv. Mater.* **2011**, *23*, 3949.

[12] T. Kim, J. Park, J. Sohn, D. Cho, S. Jeon, *ACS Nano* **2016**, *10*, 4770.

[13] C. Pang, J.H. Koo, A. Nguyen, J.M. Caves, M.-G. Kim, A. Chortos, K. Kim, P.J. Wang, J.B.-H. Tok, Z. Bao, *Adv. Mater.* **2015**, *27*, 634.

[14] A. Wasay, D. Sameoto, *Lab Chip* **2015**, *15*, 2749.

[15] C. Linghu, C. Wang, N. Cen, J. Wu, Z. Lai, J. Song, *Soft Matter* **2019**, *15*, 30.

[16] S. Wang, H. Luo, C. Linghu, J. Song, *Adv. Funct. Mater.* **2021**, *31*, 2009217.

[17] R. Hensel, K. Moh, E. Arzt, *Adv. Funct. Mater.* **2018**, *28*, 1800865.

[18] S. Li, H. Tian, J. Shao, H. Liu, D. Wang, W. Zhang, *ACS Appl. Mater. Interfaces* **2020**, *12*, 39745.

[19] H. Tian, H. Liu, J. Shao, S. Li, X. Li, X. Chen, *Soft Matter* **2020**, *16*, 5599.

[20] S. Song, D.-M. Drotlef, C. Majidi, M. Sitti, *Proc. Natl. Acad. Sci. U. S. A.* **2017**, *114*, E4344.

[21] H. Jiang, E.W. Hawkes, C. Fuller, M.A. Estrada, S.A. Suresh, N. Abcouwer, A.K. Han, S. Wang, C.J. Ploch, A. Parness, M.R. Cutkosky, *Sci. Robot.* **2017**, *2*, eaan4545.

[22] J. Jiao, F. Zhang, T. Jiao, Z. Gu, S. Wang, *Adv. Sci.* **2018**, *5*, 1700787.

[23] J. Shintake, V. Cacucciolo, D. Floreano, H. Shea, *Adv. Mater.* **2018**, *30*, 1707035.

[24] X. Li, P. Bai, X. Li, L. Li, Y. Li, H. Lu, L. Ma, Y. Meng, Y. Tian, *Friction* **2021**, https://doi.org/10.1007/s40544-021-0522-4

[25] Y. Li, J. Krahn, C. Menon, *J. Bionic Eng.* **2016**, *13*, 181.

[26] B. Aksak, M.P. Murphy, M. Sitti, *Langmuir* **2007**, *23*, 3322.

[27] D. Tao, X. Gao, H. Lu, Z. Liu, Y. Li, H. Tong, N. Pesika, Y. Meng, Y. Tian, *Adv. Funct.*

Mater. **2017**, *27*, 1606576.

[28] S. Seo, J. Lee, K.-S. Kim, K.H. Ko, J.H. Lee, J. Lee, *ACS Appl. Mater. Interfaces* **2014**, *6*, 1345.

[29] Y. Wang, R. Hensel, *Adv. Funct. Mater.* **2021**, *31*, 2101787.

[30] S.C.L. Fischer, K. Groß, O. Torrents Abad, M.M. Becker, E. Park, R. Hensel, E. Arzt, *Adv. Mater. Interfaces* **2017**, *4*, 1700292.

[31] G. Carbone, E. Pierro, S.N. Gorb, *Soft Matter* **2011**, *7*, 5545.

[32] S. Kim, M. Sitti, *Appl. Phys. Lett.* **2006**, *89*, 261911.

[33] Y. Wang, H. Hu, J. Shao, Y. Ding, *ACS Appl. Mater. Interfaces* **2014**, *6*, 2213.

[34] W. Jiang, G. Ye, B. Chen, H. Liu, *Soft Matter* **2021**, *17*, 8651.

[35] D. Son, V. Liimatainen, M. Sitti, *Small* **2021**, *17*, 2102867.

[36] A. Simaite, M. Spenko, *Bioinspir. Biomim.* **2019**, *14*, 046005.

[37] Y. Zhang, S. Ma, B. Li, B. Yu, H. Lee, M. Cai, S.N. Gorb, F. Zhou, W. Liu, *Chem. Mater.* **2021**, *33*, 2785.

[38] S.C.L. Fischer, E. Arzt, R. Hensel, *ACS Appl. Mater. Interfaces* **2017**, *9*, 1036.

[39] R.G. Balijepalli, S.C.L. Fischer, R. Hensel, R.M. McMeeking, E. Arzt, *J. Mech. Phys. Solids* **2017**, *99*, 357.

[40] S. Gorumlu, B. Aksak, *R. Soc. Open Sci.* **2017**, *4*, 161105.

[41] Q. Liu, D. Tan, F. Meng, B. Yang, Z. Shi, X. Wang, Q. Li, C. Nie, S. Liu, L. Xue, *Small* **2021**, *17*, 2005493.

[42] Z. Wang, *ACS Nano* **2018**, *12*, 1273.

[43] K. Ni, Q. Peng, E. Gao, K. Wang, Q. Shao, H. Huang, L. Xue, Z. Wang, *ACS Nano* **2021**, *15*, 4747.

[44] D. Tan, X. Wang, Q. Liu, K. Shi, B. Yang, S. Liu, Z.-S. Wu, L. Xue, *Small* **2019**, *15*, 1904248.

[45] A. Kalantari, K. Mahajan, D. Ruffatto, M. Spenko, Autonomous perching and take-off on

vertical walls for a quadrotor micro air vehicle, 2015 IEEE International Conference on Robotics and Automation (ICRA), 2015, pp. 4669.

[46] W. Wang, Y. Liu, Z. Xie, *J. Bionic Eng.* **2021**, https://doi.org/10.1007/s42235-021-00088-7

[47] J. Chen, Y. Zhu, X. Chang, D. Pan, G. Song, Z. Guo, N. Naik, *Adv. Funct. Mater.* **2021**, *31*, 2104686.

[48] T. Zhao, L. Yuan, T. Li, L. Chen, X. Li, J. Zhang, *ACS Appl. Mater. Interfaces* **2020**, *12*, 55362.

[49] D.-M. Drotlef, M. Amjadi, M. Yunusa, M. Sitti, *Adv. Mater.* **2017**, *29*, 1701353.

[50] C. Wang, Y. Fan, J. Shao, Z. Yang, J. Sun, H. Tian, X. Li, *Nano Res.* **2021**, *14*, 2606.

[51] N.J. Glassmaker, A. Jagota, C.-Y. Hui, W.L. Noderer, M.K. Chaudhury, *Proc. Natl. Acad. Sci. U. S. A.* **2007**, *104*, 10786.

[52] X. Zhang, Y. Wang, R. Hensel, E. Arzt, *J. Appl. Mech.* **2020**, *88*, 031015.

[53] Y. LIU, H. LIU, Y. GAO, *J. Mech. Med. Biol.* **2015**, *15*, 1550068.

[54] H. Hu, H. Tian, J. Shao, Y. Wang, X. Li, Y. Tian, Y. Ding, B. Lu, *Adv. Mater. Interfaces* **2017**, *4*, 1700016.

[55] V. Tinnemann, L. Hernández, S.C.L. Fischer, E. Arzt, R. Bennewitz, R. Hensel, *Adv. Funct. Mater.* **2019**, *29*, 1807713.

[56] T.L. Liu, C.-J.C. Kim, *Science* **2014**, *346*, 1096.

[57] Y. Luo, J. Shao, S. Chen, X. Chen, H. Tian, X. Li, L. Wang, D. Wang, B. Lu, *ACS Appl. Mater. Interfaces* **2019**, *11*, 17796.

[58] Y. Gao, Y. Lin, Z. Peng, Q. Zhou, Z. Fan, *Nanoscale* **2017**, *9*, 18311.

[59] M.K. Choi, H. Yoon, K. Lee, K. Shin, *Langmuir* **2011**, *27*, 2132.

[60] C.T. Bauer, E. Kroner, N.A. Fleck, E. Arzt, *Bioinspir. Biomim.* **2015**, *10*, 066002.

[61] N.J. Glassmaker, A. Jagota, C.-Y. Hui, J. Kim, *J. R. Soc. Interface* **2004**, *1*, 23.

[62] C.Y. Hui, A. Jagota, Y.Y. Lin, E.J. Kramer, *Langmuir* **2002**, *18*, 1394.

[63] A. Jagota, S.J. Bennison, *Intergr. Comp. Biol.* **2002**, *42*, 1140.

[64] Y.-T. Cheng, C.-M. Cheng, *J. Appl. Phys.* **1998**, *84*, 1284.

[65] H. Hu, S. Zhao, W. Wang, Y. Zhang, Y. Fu, Z. Zheng, *Appl. Phys. Lett.* **2021**, *119*, 071603.

[66] V. Barreau, R. Hensel, N.K. Guimard, A. Ghatak, R.M. McMeeking, E. Arzt, *Adv. Funct. Mater.* **2016**, *26*, 4687.

[67] B.N. Persson, *Phys. Rev. Lett.* **2002**, *89*, 245502.

[68] H. Yao, H. Gao, *Int. J. Solids Struct.* **2007**, *44*, 8177.

[69] R. Long, C.-Y. Hui, S. Kim, M. Sitti, *J. Appl. Phys.* **2008**, *104*, 044301.

[70] X. He, Q. Li, V.L. Popov, *J. Adhes.* **2021**, 1. https://doi.org/10.1080/00218464.2021.1939017

[71] F. Jin, X. Guo, H. Gao, *J. Mech. Phys. Solids* **2013**, *61*, 2473.

[72] L. Bauman, Q. Wen, D. Sameoto, C.H. Yap, B. Zhao, *Colloids Surf. Physicochem. Eng. Asp.* **2021**, *610*, 125901.

[73] D. Sameoto, C. Menon, *J. Micromech. Microeng.* **2009**, *19*, 115002.